Soil Dynamics and Earthquake Engineering 166 (2023) 107760

Contents lists available at ScienceDirect

Soil Dynamics and Earthquake Engineering

journal homepage: www.elsevier.com/locate/soildyn

An optimization-based rigid block modeling approach to seismic assessment of dry-joint masonry structures subjected to settlements

F.P.A. Portioli [a,*], L. Cascini [a], R. Landolfo [a], P.B. Lourenço [b]

[a] Dept. of Structures for Engineering and Architecture, University of Naples Federico II, Via Forno Vecchio 36, 80134, Naples, Italy
[b] Department of Civil Engineering, ISISE, University of Minho, Guimarães, Portugal

ARTICLE INFO

Keywords:
Rigid block modeling
Dry-joint masonry
Settlements
Seismic actions
Non-linear static analysis
Time-history analysis
Rocking behavior

ABSTRACT

A rigid block modeling approach is presented for rocking dynamics and nonlinear static analysis of dry-joint masonry structures subjected to settlements and earthquake excitations. For the different types of analysis, a unified optimization-based formulation is adopted, which is equivalent to the system governing the static and dynamic structural response. Sequential solution procedures are used for time integration and for pushover analysis which take into account the effects of large displacements under the combined action of support movements and lateral loads. No-tension elastic contacts with finite shear strength are considered at block interfaces for time-history analysis and to obtain the elastic branch of pushover curves in nonlinear static analysis. A unilateral rigid contact behavior is also considered to obtain the descending post-peak branch of pushover curves corresponding to the activation of the rigid-body rocking motion, according to displacement-based assessment methods of failure mechanisms adopted in the standards. Comparisons with numerical models and experimental tests on a rocking block and on a buttressed arch are presented to show the accuracy of the developed approach. Simple tests on dry-joint tuff panels on the tilting table were also carried out to show the effects of imposed movements at support on the response to lateral loads. Finally, an application is presented to a full-scale triumphal arch subjected to the combined action of support movements and earthquake excitation to discuss, on the basis of the developed model, the effects of settlement-induced damage on seismic performance. The numerical analyses showed that the lateral force, the displacement capacity and the rocking response can be significantly affected by support movements, pointing out the relevance of the current building condition in the seismic safety assessment.

1. Introduction

In several European countries, the built cultural heritage is exposed to different types of natural and anthropic hazards. Among those, earthquakes and settlements represent frequent causes of damage on structures. In addition to the wide scientific literature on the effect of earthquakes on structures, there are also many studies that investigate the structural behavior and damage induced by foundation settlements, such as [1] for tunneling, [2] for soft soils and [3–5] for slow-moving landslides. In a few circumstances, structures could be damaged by a succession of events, for example in the case of earthquakes acting on buildings which have been previously subjected to foundation settlements. Therefore, there is the need to assess the vulnerability against the combined effects of these actions.

Within this framework, just a few studies in the literature have addressed the issue of the seismic assessment of buildings affected by ground movements. Fragility curves for reinforced concrete buildings subject to seismically triggered slow-moving landslides were developed in Ref. [6]. A procedure for seismic safety assessment of reinforced concrete buildings based on nonlinear static analysis of the deformed configuration obtained from satellite data was presented in Ref. [7]. Seismic fragility curves of historic masonry buildings subject to settlement induced damage were developed in Refs. [8,9]. In both cases, the seismic assessment was carried out using nonlinear static analysis and adopting a macro-modeling approach [10]. The approach takes into account the in-plane behavior of masonry panels which is generally associated to a box type behavior of the buildings. This kind of behavior is related to stiff floors and strong connections which are able to provide diaphragm actions and to exploit the in-plane strength of masonry panels [11].

* Corresponding author.
E-mail address: fportiol@unina.it (F.P.A. Portioli).

https://doi.org/10.1016/j.soildyn.2023.107760
Received 23 June 2022; Received in revised form 12 December 2022; Accepted 2 January 2023
Available online 12 January 2023

However, when the connections are weak and the diaphragms are missing or flexible, as is common in the case of historic masonry buildings, the seismic behavior can be affected by local out-of-plane failure mechanisms which generally exhibit a rocking behavior [12]. Local failure mechanisms are also exacerbated by thrusts induced by curved elements, such as arches, vaults and domes, which represent a typical feature of masonry built cultural heritage.

The effects related to the thrust of arches and vaults on seismic capacity of failure mechanisms could be even more detrimental when structures are also subjected to settlements, which are generally associated to vertical and horizontal movements, also leading to rotations. The displacement capacity of arched structures subjected to settlement is very large and has been investigated in different studies on the basis of experimental tests and numerical analyses [13,14]. Applications based on sequential limit analysis can be found in Refs. [15–18], whereas examples of combinatorial analysis for the identification of the failure mechanisms analyzed in the large displacement regime are reported in Refs. [19,20]. However, evaluating the effects of ground movements on the seismic capacity of local failure mechanisms is still an open issue.

The present study focuses on the development of a novel discrete modeling approach for the seismic analysis of local failure mechanisms in dry-joint historic masonry structures which have been previously subjected to foundation settlement. The approach comprises different analysis types for the vulnerability assessment of local failure mechanisms, according to the standards. The analysis types include limit equilibrium analysis (or linear kinematic analysis), nonlinear static (i.e., pushover) analysis and dynamic analysis. For each analysis type, the proposed approach includes the capability to take into account the effects of support movement on the force and displacement capacity against seismic actions.

In the literature, both continuous and discontinuous, micro and macro modeling approaches have been developed for the static and dynamic analysis of failure mechanisms in historic masonry structures [21,22]. Examples of modeling approaches based on finite element method (FEM) can be found in Refs. [23–27]. Finite element and rigid block models based on limit analysis were developed in Ref. [28] and in Refs. [29–34]. Rigid block models for rocking dynamics were presented in Refs. [35–37]. Rigid body spring models (RBSM) and modeling approaches based on the applied element method (AEM) were developed in Refs. [38–41]. Modeling approaches and tools based on combined strategies, multi-step procedures and analytical formulations were presented in Refs. [42–46]. Distinct element method (DEM) has been also conveniently and widely applied to the analysis of historic masonry structures [47–52].

The proposed rigid block modeling approach for limit equilibrium analysis, nonlinear static and dynamic analysis represents an alternative to classic DEM and discontinuous FEM. Similar to classic methods of limit analysis [53–58] and contact dynamics [59–61], the developed modeling approach is based on the use of an optimization-based formulation, which is equivalent to the system of equations governing the structural response, on the use of gap functions to express non-penetration conditions and on the use of simple algorithms for the specification of potential contacts.

A characteristic feature of the adopted modeling approach is that the problems for rocking dynamics and nonlinear static analysis in limit analysis are formulated within a unified framework using a special class of mathematical programming problem, that is the linear complementarity problem, which arises from the set of equalities and inequalities corresponding to equilibrium, geometric compatibility, failure and complementarity conditions [62]. Complementarity conditions are the distinct feature of the problem and are used to impose the activation of contact displacement rates at failure as well as non-penetration conditions, adopting the classic form used for limit analysis and contact dynamics by mathematical programming.

Formulating the modeling approach in terms of a linear complementarity problem is convenient in different ways if compared to other discrete models such as the classic DEM. The problems can be uncoupled into dual equivalent displacement and force-based optimization problems, corresponding to the lower and upper bound formulation in the case of limit analysis problems, for which very efficient and robust solvers are available [63,64]. The solution to the problems satisfies both equilibrium, geometric compatibility, failure and non-penetration conditions, with no need to alternate between the contact forces at interfaces and the dynamic equilibrium of the blocks. By means of gap functions and simple schemes for the specification of potential contact points, the size of the numerical problems associated to the unknown contact forces does not change with large displacements from the initial configuration. This noteworthy feature allows to significantly simplify the implementation of the numerical problems. Formulations for static analysis can be simply derived from dynamic analysis, by omitting the contribution of inertia forces with no need to introduce artificial damping, as it is the case of DEM. Finally, expressing the behavior of rigid contacts by means of complementarity conditions allows to avoid the use of arbitrary large stiffness at the joints, as it is usually done in the case of DEM to reproduce infinite contact stiffness. On the other hand, in the proposed modeling approach the dissipation is implicitly related to the algorithm used for time integration and to mechanical parameters, as discussed in Ref. [65] and also shown in the sensitivity analyses reported in the following.

With respect to the authors' previous work, the novel contribution of this study is twofold. Previous developed modeling approaches for 2D analysis under imposed movements [66,67] or lateral loads [68] are herein extended to the case of combined settlement and seismic actions, both for static and dynamic regimes. Moreover, no-tension elastic contacts are also included for time-history analysis, whereas rigid contacts were considered in previous works for rocking dynamics [69]. The developed formulations are presented following the unified framework adopted in Ref. [65], now showing that the different analysis types (limit equilibrium analysis, pushover static and time-history analysis) can be derived as special cases of dynamic formulation with elastic contacts. The new formulations have been collected in a software package which is available for applications.

The manuscript is organized as follows. In Sect. 2 the different analysis types and the actions modeling are described. The optimization-based formulation implemented for the different analysis types and sequential solution procedures are presented in Sect.3 and 4. In Sect. 5 the results of nonlinear static analysis on selected cases studies are presented to discuss the effects of support movements on the capacity to lateral loads. The case studies comprise a buttressed arch and a dry-joint tuff masonry panel tested on the tilting table against support movement and lateral loads. Comparisons with numerical and experimental tests on single and multi-block structures subjected to free rocking motion, pulse and earthquake excitation are shown in Sect. 6 to validate the proposed modeling approach with no-tension elastic contacts in the dynamic regime. An application to the evaluation of settlements-induced damage on the seismic response of a full-scale triumphal arch is presented in Sect.7, where a comparison is carried out between static and dynamic assessment methods following the provisions contained in the Italian technical standard [70,71].

2. Rigid block model, actions modeling and analysis types

In the proposed modeling approach, rigid blocks i are assumed to interact via no-tension, frictional contact interfaces j. Each interface j comprises two surfaces s and four contact points k – corresponding to the end points of the surfaces – where normal and shear contact forces n_k and t_k are applied (Fig. 1a and b). Failure modes occur at contact interfaces and include opening and sliding. As for contact stiffness, both rigid and unilateral elastic contacts are used for the analysis.

The model is formulated in the dynamic regime for seismic actions, considering unilateral elastic contacts and taking into account the effects of large displacements (i.e., P-Δ effects) on the structural response.

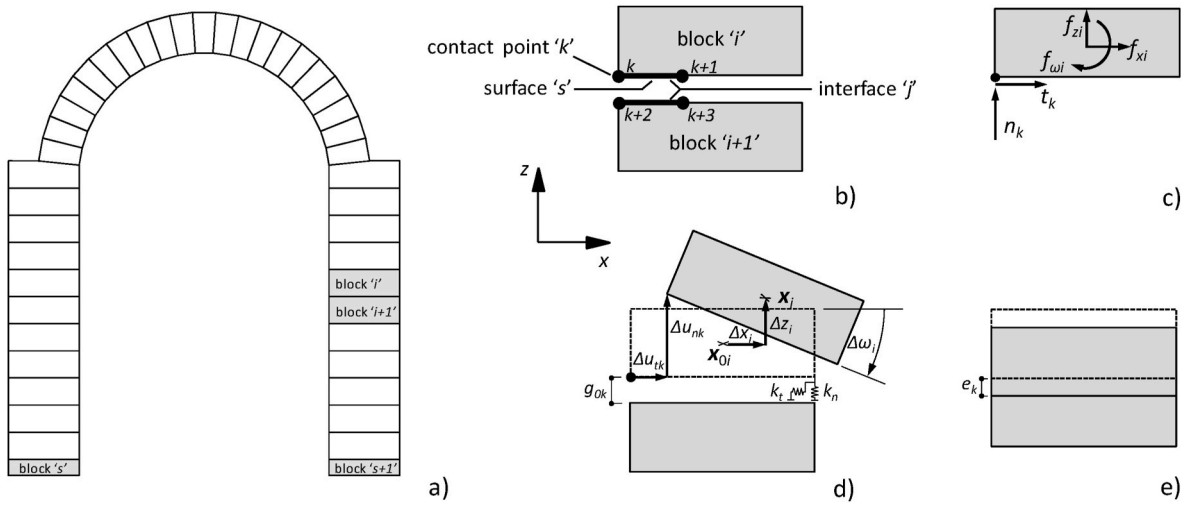

Fig. 1. Formulation of the model: a) Rigid block model of a dry joint buttressed arch generated in AutoCAD using polylines; b) contact points, surfaces and interfaces at blocks i and i+1; c) contact and external forces; d) block and contact displacements, contact gaps and stiffness; e) interpenetration at contact point associated to elastic behavior.

Earthquake excitations are applied at support (or base) blocks s and are expressed in terms of acceleration time histories $a_g(t)$ (Figs. 1a and 2a).

A static formulation which is derived from dynamics by simply neglecting the inertia forces is adopted to model the effects of settlements. The two formulations (static and dynamic) can be used in sequence to evaluate the effects of settlements on the rocking response under seismic actions. In this study, settlements are modelled with movable support blocks with a single degree of freedom, corresponding

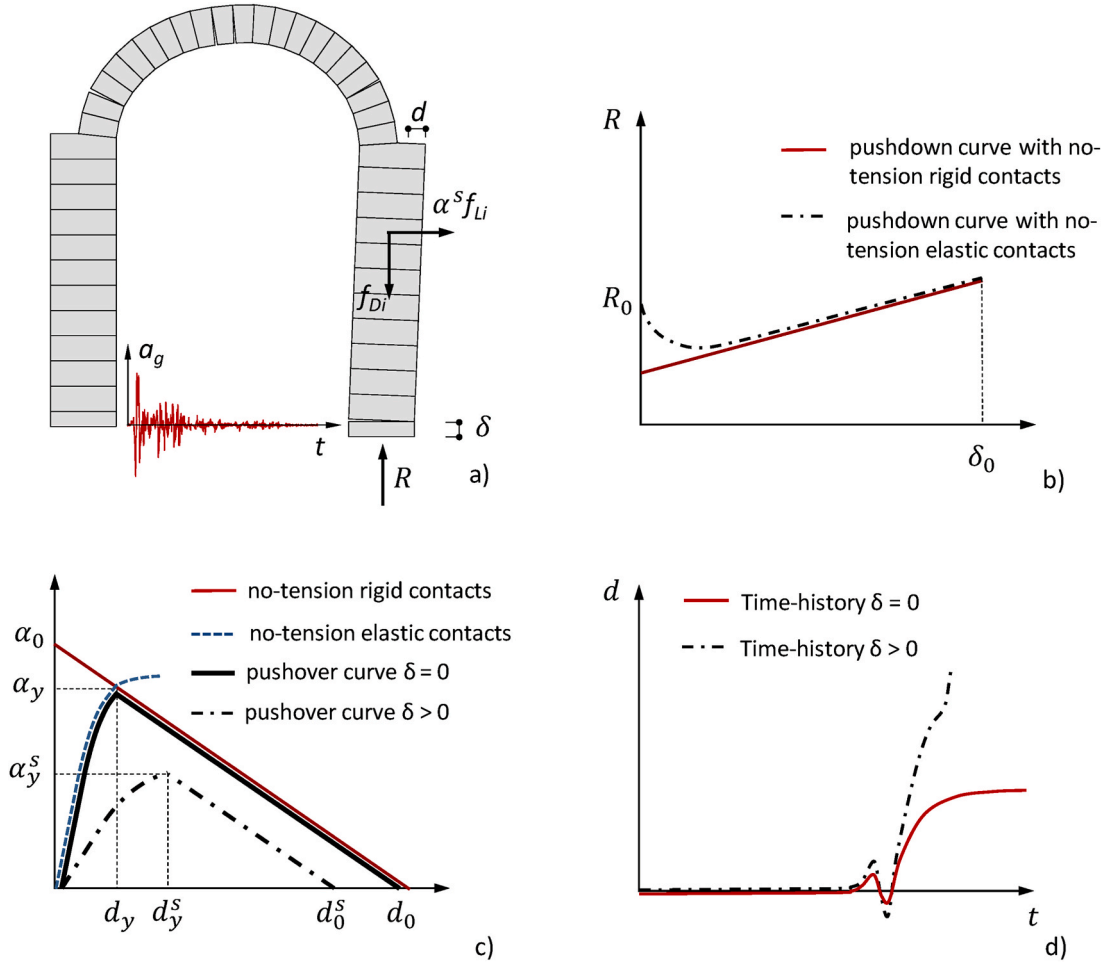

Fig. 2. Different types of analysis and results: a) Load configurations, control displacements and imposed movements for nonlinear static and time history analysis; b) Response curves obtained from pushdown analysis; c) pushover curves and d) displacement time history curves obtained from nonlinear static and dynamic analysis for the original and settled configurations.

to vertical, horizontal or inclined movements δ (Fig. 2a).

An integrated full-static formulation was also implemented to evaluate the effects of settlements on the evolution of failure mechanisms associated to lateral loads. This formulation is devoted to the nonlinear kinematic analysis of local failure mechanisms, according to the Italian technical standard. The seismic actions are represented in this case with a uniform distribution of lateral loads $\alpha \boldsymbol{f_L}$, expressed as a factor of vertical dead loads $\boldsymbol{f_D}$ (Fig. 2a). The response to lateral loads of the failure mechanism is characterized in this case by a pushover curve, expressing the variation of the load multiplier α as a function of a control point displacement d (Fig. 2a, c). Following the approach presented in Ref. [68], the pre-peak response is obtained assuming a unilateral elastic behavior at contacts. The descending branch of the pushover curve corresponding to the post-peak behavior is obtained using a sequential solution procedure based on the limit equilibrium analysis of the displaced configuration, so to take into account the effects of large displacements on the value of the load multiplier. To capture the post-peak response in the pushover curve, a rigid behavior is assumed at contacts, according to the approach for nonlinear kinematic analysis of failure mechanisms contained in the Italian technical standard.

As such, the proposed modeling approach includes the following analysis types, with rigid or elastic contacts, which can be carried out in sequence to take into account the effects of settlements on the seismic capacity: pushdown analysis with movable support blocks (Fig. 2b); pushover analysis under lateral loads (Fig. 2c); time-history analysis under seismic excitation (Fig. 2d). The analyses return the failure modes and the deformed configurations, as well as the response curves in terms of a control force and displacement. In the case of pushdown analysis, the curves report the reaction R at the moving support as a function of the support movement δ. The response parameters obtained from the pushover curves for lateral loads are: the lateral load multipliers at the onset of motion α_0 for rigid contacts; the load multiplier at the force capacity α_y and the displacement d_y corresponding to no-tension elastic contact behavior, and the ultimate displacement d_0. Corresponding response parameters obtained from pushover analysis on the configuration subjected to support movements are indicated with apex s in Fig. 2c. Relative displacements at control points are evaluated in this case with respect to the deformed configuration subjected to settlement. Finally, the response parameter obtained from the time history analysis is the control displacement(s) as a function of time.

A MATLAB® application was developed on the basis of the proposed approach which was organized into a main file and three functions for the generation of the numerical model and the assembly of matrices underlying the numerical problems associated to each analysis type, for the analysis and for the output. The tool comes with a simple input interface, which is organized using an Excel spreadsheet. The geometry of the block assemblage can be imported from DXF files. Geometric models are made of closed polylines corresponding to the blocks. Surfaces s correspond to the edges of the polylines (Fig. 1a) The number of contact point per each surface can be refined to increase the accuracy, simply by using multiple lines per each edge. A routine was developed to calculate from CAD polylines the geometric and mass properties which are needed for the analysis.

3. Optimization-based nonlinear static analysis and rocking dynamics

The integrated rigid block modeling approach relies on the following general matrix form for the system of equations, inequalities and complementarity conditions which govern the dynamics of a rigid block assemblage with no-tension elastic contacts:

$$\begin{bmatrix} \overline{\boldsymbol{M}} & . & \boldsymbol{A_0} \\ . & . & -\boldsymbol{Y}^{\mathrm{T}} \\ -\boldsymbol{A_0}^{\mathrm{T}} & \boldsymbol{Y} & \boldsymbol{C} \end{bmatrix}_{n\times n} \begin{bmatrix} \Delta \boldsymbol{x} \\ \boldsymbol{\lambda} \\ \boldsymbol{c} \end{bmatrix}_{n\times 1} + \begin{bmatrix} . \\ \boldsymbol{y} \\ . \end{bmatrix} = \begin{bmatrix} \overline{\boldsymbol{f}} \\ -\boldsymbol{r} \\ -\boldsymbol{g_0} \end{bmatrix} \quad \text{s.t.} \quad \boldsymbol{y} \le \boldsymbol{0} \quad \boldsymbol{\lambda} \ge \boldsymbol{0} \quad \boldsymbol{y}^{\mathrm{T}}\boldsymbol{\lambda} = 0 \tag{1}$$

where.

$\Delta \boldsymbol{x}$: is the $(3b \times 1)$ vector collecting unknown displacement rates Δx_i, Δz_i and $\Delta \omega_i$ at block centroids, being b the number of blocks (Fig. 1d);
$\boldsymbol{\lambda}$: is the $(3c \times 1)$ vector of non-negative flow multipliers of contact displacement rates at failure, being c the number of contact points;
$\boldsymbol{c}$: is the $(2c \times 1)$ vector of the unknown normal and tangential contact forces n_k and t_k acting at contact points k;
$\boldsymbol{A_0}$: is the $(3b \times 2c)$ equilibrium matrix at time t_0;
$\boldsymbol{C}$: is the $(2c \times 2c)$ diagonal matrix of contact compliances $C_{kn} = 1/k_n$ and $C_{kt} = 1/k_t$;
$\overline{\boldsymbol{M}}$: is the $(3b \times 3b)$ diagonal matrix of scaled masses;
$\boldsymbol{Y}$: is the flow rule matrix of contact displacement rates at failure;
$\overline{\boldsymbol{f}}$: is the $(3b \times 1)$ vector of external scaled forces at time t_0;
$\boldsymbol{g_0}$: is the $(2c \times 1)$ vector of contact gaps g_{0k} and initial known tangential displacement rates $C_{kt}t_{0k}$ at contact points;
$\boldsymbol{r}$: is the vector of constant terms associated to failure conditions;
$\boldsymbol{y}$: is the vector of failure conditions.

The three rows of the problem defined in Eq. (1) with size $n = 3b+3c+2c$ provide equilibrium, failure and kinematic compatibility conditions, respectively.

The equations $\overline{\boldsymbol{M}}\Delta \boldsymbol{x} + \boldsymbol{A_0}\boldsymbol{c} = \overline{\boldsymbol{f}}$ governing the dynamic equilibrium of rigid blocks are obtained from the application of a time stepping scheme to the integration of the equilibrium conditions expressed at the acceleration level. The implicit Euler method is used, posing at time $t = t_0 + \Delta t$: $\boldsymbol{a}(t) = \frac{\boldsymbol{v}-\boldsymbol{v_0}}{\Delta t}$; $\boldsymbol{v}(t) = \frac{\Delta \boldsymbol{x}}{\Delta t}$; $\overline{\boldsymbol{M}} = \frac{1}{\Delta t^2}\boldsymbol{M}$; $\overline{\boldsymbol{f}} = \boldsymbol{f} + \overline{\boldsymbol{M}}\boldsymbol{v_0}\Delta t$, where: $\boldsymbol{f}$ is the vector of external forces; $\boldsymbol{M}$ is the diagonal mass matrix, collecting mass m_i and mass moment of inertia J_i of blocks i and $\boldsymbol{v_0}$ is the known velocity at time t_0. Vector $\boldsymbol{f}$ collects subvectors of external forces at block i (with vertical loads $f_{zi} = -m_i g$, being g the acceleration of gravity) and external forces at support blocks s (with horizontal forces $f_{xs} = m_s a_g(t)$ associated to earthquake excitation, being m_s the mass of support blocks). For the calculation of contact gaps g_{0k} and of the equilibrium matrix entries, the four-points scheme adopted in Refs. [65,67] was used.

The general expression adopted in Eq. (1) for failure conditions $\boldsymbol{y} = \boldsymbol{Y}^{\mathrm{T}}\boldsymbol{c} - \boldsymbol{r} \le \boldsymbol{0}$ refers to opening, sliding (through the matrix of failure conditions $\boldsymbol{Y}^{\mathrm{T}}$, expressed as a function of the friction coefficient μ) and crushing failure at contact points, through the constant vector $\boldsymbol{r}$ [68]. For the applications presented in this study, an infinite compressive strength is assumed and $\boldsymbol{r}$ is a null vector.

Kinematic compatibility conditions $\boldsymbol{A_0}^{\mathrm{T}}\Delta \boldsymbol{x} = \boldsymbol{Y}\boldsymbol{\lambda} + \boldsymbol{C}\boldsymbol{c} + \boldsymbol{g_0}$ correspond to the condition that displacement rates $\Delta \boldsymbol{u}$ at contact points, expressed as a function of displacement rates at blocks centroids according to contragradience principle (i.e. $\Delta \boldsymbol{u} = \boldsymbol{A_0}^{\mathrm{T}}\Delta \boldsymbol{x}$), are equal to the displacement rates expressed as a function of displacement flow rule at failure ($\boldsymbol{Y}\boldsymbol{\lambda}$), of elastic deformations at contacts ($\boldsymbol{e} = \boldsymbol{C}\boldsymbol{c}$) and of initial gaps and known tangential displacement rates ($\boldsymbol{g_0}$).

Complementarity conditions $\boldsymbol{y}^{\mathrm{T}}\boldsymbol{\lambda} = 0$ ensure that displacement rates associated to flow multipliers $\boldsymbol{\lambda}$ occur only when failure conditions are attained ($\boldsymbol{y} = \boldsymbol{0}$).

The problem defined in Eq. (1) is a linear complementarity problem (LCP), which is equivalent to the two dual quadratic optimization problems [72]:

$$\begin{aligned} \min \quad & \frac{1}{2}\Delta \boldsymbol{x}^{\mathrm{T}}\,\overline{\boldsymbol{M}}\Delta \boldsymbol{x}+\frac{1}{2}\mathbf{e}^{\mathrm{T}}\,\boldsymbol{K}\mathbf{e}+\boldsymbol{r}^{\mathrm{T}}\boldsymbol{\lambda}-\overline{\boldsymbol{f}}^{\mathrm{T}}\Delta \boldsymbol{x} \\ \text{s.t.} \quad & \Delta \boldsymbol{u}=\boldsymbol{A}_{\mathbf{0}}^{\mathrm{T}}\,\Delta \boldsymbol{x} \\ & \Delta \boldsymbol{u}=\boldsymbol{Y}\boldsymbol{\lambda}+\boldsymbol{e}+\boldsymbol{g}_{\mathbf{0}},\ \boldsymbol{\lambda}\geq \mathbf{0} \end{aligned} \tag{2}$$

$$\begin{aligned} \max \quad & -\frac{1}{2}\boldsymbol{i}^{\mathrm{T}}\,\overline{\boldsymbol{M}}^{-1}\boldsymbol{i}-\frac{1}{2}\boldsymbol{c}^{\mathrm{T}}\,\boldsymbol{C}\boldsymbol{c}-\boldsymbol{g}_{\mathbf{0}}^{\mathrm{T}}\boldsymbol{c} \\ \text{s.t.} \quad & \boldsymbol{i}+\boldsymbol{A}_{\mathbf{0}}\boldsymbol{c}=\overline{\boldsymbol{f}} \\ & \boldsymbol{y}\leq \mathbf{0},\ \boldsymbol{y}=\boldsymbol{Y}^{\mathrm{T}}\boldsymbol{c}-\boldsymbol{r} \end{aligned} \tag{3}$$

where $\boldsymbol{i}=\overline{\boldsymbol{M}}\Delta \boldsymbol{x}$ is the vector of inertia forces. The optimization problems defined in Eqs. (2) and (3) are the novel problems which were formulated in this study for time-history analysis with no-tension elastic contacts (Fig. 2d). The problems reduce to the form adopted in the case of dynamics with rigid contact presented in Ref. [65] by simply omitting the terms related to contact stiffness.

On the basis of the dynamic formulation for no-tension elastic contacts, the following optimization problems are derived for pushover analysis with elastic and rigid contacts, respectively (Fig. 2c):

$$\begin{aligned} \max \quad & -\frac{1}{2}\boldsymbol{c}^{\mathrm{T}}\,\boldsymbol{C}\boldsymbol{c}-\boldsymbol{g}_{\mathbf{0}}^{\mathrm{T}}\boldsymbol{c} \\ \text{s.t.} \quad & \boldsymbol{A}_{\mathbf{0}}\boldsymbol{c}=\boldsymbol{f} \\ & \boldsymbol{y}\leq \mathbf{0},\ \boldsymbol{y}=\boldsymbol{Y}^{\mathrm{T}}\boldsymbol{c} \end{aligned} \tag{4}$$

$$\begin{aligned} \max \quad & \alpha\gamma-\boldsymbol{g}_{\mathbf{0}}^{\mathrm{T}}\boldsymbol{c} \\ \text{s.t.} \quad & \boldsymbol{A}_{\mathbf{0}}\boldsymbol{c}=\boldsymbol{f}_{\boldsymbol{D}}+\alpha \boldsymbol{f}_{\boldsymbol{L}} \\ & \boldsymbol{y}\leq \mathbf{0},\ \boldsymbol{y}=\boldsymbol{Y}^{\mathrm{T}}\boldsymbol{c}-\boldsymbol{r} \end{aligned} \tag{5}$$

where external loads $\boldsymbol{f}$ are equal to $\boldsymbol{f}_{\boldsymbol{D}}+\alpha \boldsymbol{f}_{\boldsymbol{L}}$, being $\boldsymbol{f}_{\boldsymbol{D}}$ the vector of vertical dead loads and $\boldsymbol{f}_{\boldsymbol{L}}$ the vector of lateral live loads (set equal to the values of vertical loads). α is the live load multiplier, which represents an additional unknown in the solution of problem defined by Eq. (5) with rigid contacts, corresponding to the onset of motion of the failure mechanisms. γ is a constant term corresponding to the work done by lateral loads ($\boldsymbol{f}_{\boldsymbol{L}}^{\mathrm{T}}\Delta \boldsymbol{x}=\gamma$), according to Ref. [73].

Displacements at moving supports for pushdown analysis were introduced on the basis of the following displacement-based optimization problems in the case of elastic and rigid contacts, respectively (Fig. 2b):

$$\begin{aligned} \min \quad & \frac{1}{2}\mathbf{e}^{\mathrm{T}}\,\boldsymbol{K}\mathbf{e}-\boldsymbol{f}^{\mathrm{T}}\Delta \boldsymbol{x} \\ \text{s.t.} \quad & \Delta \boldsymbol{u}=\boldsymbol{A}_{\mathbf{0}}^{\mathrm{T}}\,\Delta \boldsymbol{x} \\ & \Delta \boldsymbol{u}=\boldsymbol{Y}\boldsymbol{\lambda}+\boldsymbol{e}+\boldsymbol{g}_{\mathbf{0}},\ \boldsymbol{\lambda}\geq \mathbf{0} \end{aligned} \tag{6}$$

$$\begin{aligned} \min \quad & \boldsymbol{r}^{\mathrm{T}}\boldsymbol{\lambda}-\boldsymbol{f}_{\boldsymbol{D}}^{\mathrm{T}}\Delta \boldsymbol{x} \\ \text{s.t.} \quad & \boldsymbol{f}_{\boldsymbol{L}}^{\mathrm{T}}\Delta \boldsymbol{x}=\gamma \\ & \Delta \boldsymbol{u}=\boldsymbol{A}_{\mathbf{0}}^{\mathrm{T}}\Delta \boldsymbol{x} \\ & \Delta \boldsymbol{u}=\boldsymbol{Y}\boldsymbol{\lambda}+\boldsymbol{g}_{\mathbf{0}},\ \boldsymbol{\lambda}\geq \mathbf{0} \end{aligned} \tag{7}$$

where live loads $\boldsymbol{f}_{\boldsymbol{L}}$ are associated to the varying reaction at support in problem defined by Eq. (7).

It is worth noting that problems defined by Eqs. (6) and (7) are expressed in the dual form of problems defined in Eqs. (4) and (5). Problems defined by Eqs. (4)–(7) are special cases of the generalized optimization problems defined in Eqs. (2) and (3) which can be obtained when the scaled mass matrix $\overline{\boldsymbol{M}}$ and the matrix of contact compliances $\boldsymbol{C}$ are omitted and when the additional unknown load multiplier α and the condition $\boldsymbol{f}_{\boldsymbol{L}}^{\mathrm{T}}\Delta \boldsymbol{x}=\gamma$ are introduced.

4. Sequential and time stepping solution procedures

The sequential solution procedures for pushdown and pushover analysis were organized into displacement increments $\Delta \boldsymbol{x}$ as follows.

For pushdown analysis with elastic contacts, a solution to Eq. (6) is found starting from the initial known configuration $\boldsymbol{x}_{\mathbf{0}}$, contact gaps $\boldsymbol{g}_{\mathbf{0}}$, compatibility matrix $\boldsymbol{A}_{\mathbf{0}}^{\mathbf{T}}$ and under the additional constraints corresponding to the imposed movements at support block. New positions of the blocks $\boldsymbol{x}=\boldsymbol{x}_{\mathbf{0}}+\Delta \boldsymbol{x}$, contact gaps $\boldsymbol{g}$ and the compatibility matrix $\boldsymbol{A}^{\mathbf{T}}$ are determined and a new optimization problem (6) is set up and solved on the basis of the updated configuration.

Once the final imposed displacement is applied at the support block, the procedure switches to the solution of force-displacement problem defined by Eq. (4) for pushover analysis. The solution starts from the deformed configuration under the imposed movement at support block to obtain contact forces $\boldsymbol{c}$ under a given distribution of external forces $\boldsymbol{f}=\boldsymbol{f}_{\boldsymbol{D}}+\alpha \boldsymbol{f}_{\boldsymbol{L}}$, with the lateral loads being expressed as a function of a known, increasing multiplier α. Displacements $\Delta \boldsymbol{x}$ corresponding to the dual problem in Eq. (6) are recovered from the Lagrange multipliers associated to the solution of the same force-based problem in Eq. (4).

A similar procedure was implemented for pushdown and pushover analysis with rigid contacts solving problems defined by Eqs. (7) and (5).

The time stepping algorithm used for time history analysis was organized into time increments Δt. A solution to problem in Eq. (3) is obtained in terms of contact forces $\boldsymbol{c}$ and inertia forces $\boldsymbol{i}$ starting from contact gaps $\boldsymbol{g}_{\mathbf{0}}$, equilibrium matrix $\boldsymbol{A}_{\mathbf{0}}$ and external forces $\overline{\boldsymbol{f}}=\boldsymbol{f}+\overline{\boldsymbol{M}}\boldsymbol{v}_{\mathbf{0}}\Delta t$ corresponding to the configuration $\boldsymbol{x}_{\mathbf{0}}$ and velocities $\boldsymbol{v}_{\mathbf{0}}$ at time t_0. The configuration $\boldsymbol{x}=\boldsymbol{x}_{\mathbf{0}}+\Delta \boldsymbol{x}$, velocities $\boldsymbol{v}$, external forces $\overline{\boldsymbol{f}}$ and equilibrium matrix $\boldsymbol{A}$ at time $t_0+\Delta t$ are updated on the basis of displacements $\Delta \boldsymbol{x}$ corresponding to problem in Eq. (2) which are directly obtained from Lagrange multipliers associated to the solution of problem in Eq. (3). Then, a new optimization problem defined by Eq. (3) is formulated and solved on the basis of the updated configuration.

For the solution of problems in Eqs. (2)–(7), the MOSEK optimization toolbox for MATLAB was used (ver 9.1.10). For the simulations presented in this study, an infinite compressive strength and a rigid behavior for tangential displacements at contact points were considered. As such, in problems defined in Eqs. (2)–(7), $\boldsymbol{r}$ is the null vector and tangential contact compliances C_{kt} were set equal to 0. Considering that a four-point contact model was assumed at each interface j, the normal compliances $C_{kn}=1/k_n$ at contact points were determined on the basis of joint stiffness k_{jn}, adopting the following expression for contact stiffness: $k_n=(k_{jn}\bullet l_j\bullet d_j)/4$, being l_j and d_j the length and the depth at joint j. The constant term γ corresponding to the work done by live loads in Eqs. (5) and (7) was set in the range 0.01–100 kNm.

5. Effects of support movements on pushover curves: analytical and experimental comparisons

Nonlinear static analysis under support movements and lateral loads are carried out in sequence to evaluate the capability of the proposed approach in predicting the effects of settlements on the pushover curves. Two case studies are considered, namely a buttressed arch and a dry-joint tuff masonry panel. The geometric configuration of the buttressed arch is the one experimentally investigated for lateral loads on the tilting and shaking table in Refs. [74,75]. In this case a comparison is carried out in terms of pushover curves between the proposed approach and the analytical and experimental responses. As for the tuff masonry panel, tilting table tests were carried out for comparisons with results of nonlinear static analysis with rigid contacts. The panel was tested in two different configurations, without and with imposed displacements at the base, in order to evaluate the effects of support movements on the failure modes and on the lateral loads promoting the collapse mechanism.

5.1. Buttressed arch subjected to combined settlement and lateral loads

The configuration of the arch considered is shown in Fig. 3a). The

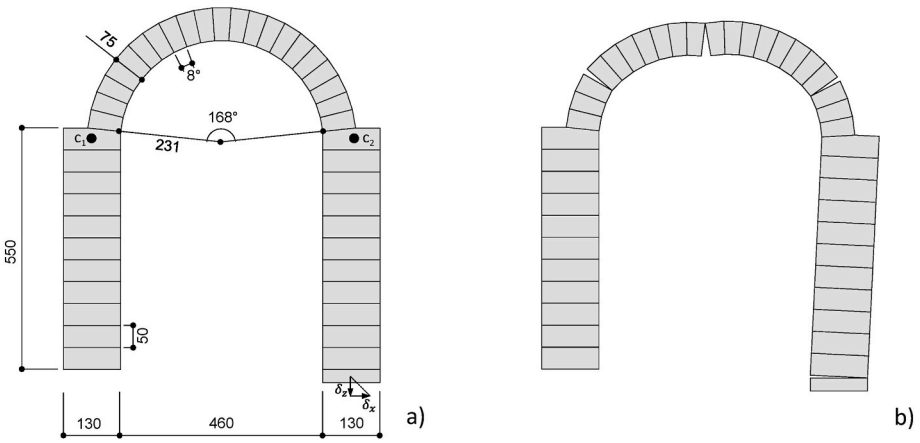

Fig. 3. Buttressed arch: a) Rigid block model; b) Displaced configuration with rigid contacts under support movement and lateral loads at ultimate displacement ($\delta_x = \delta_z = 20$ mm, $d_0^s = 24.7$ mm).

depth of the arch is 100 mm. The unit weight of the blocks is 11.5 kN/m^3, the friction coefficient is equal to 0.6 and the joint stiffness k_{jn} is equal to 1.2e5 kN/m^3, according to Ref. [75]. The joints between the blocks along the piers and the arch were discretized with eight and four contact interfaces, respectively.

A pushdown analysis was first carried out to evaluate the displacement capacity of the system under imposed movements. The movement was applied at the support block on the right side with equal vertical and horizontal displacement. The pushdown curves plotting the horizontal component of the thrust R_x versus the horizontal movement δ_x are shown in Fig. 4a), both for rigid and elastic contacts. The results show that the deformability of the joints significantly affects the displacement capacity of the system, with ultimate displacements equal to 65.0 mm and 27.0 mm in the case of rigid and elastic contacts, respectively. This is in accordance with the results reported in Refs. [76,77], where it is shown that contact stiffness strongly influences the ultimate displacement of arches subject to inclined support movements.

Sequential pushdown and pushover analysis were then carried out to evaluate the effects on the pushover curve. The buttressed arch was first subjected to a horizontal and vertical displacement of 20.0 mm at the right support (Fig. 3b). Displacement increments of 1.0 mm were applied at the support block for pushdown analysis. In the case of rigid contacts, the reaction obtained at moving support and the displacement at control point C_2 corresponding to the imposed movements of 20.0 mm were equal to 10.4 N and 22.5 mm, respectively. For no-tension elastic contacts, corresponding values of 10.9 N and 24.4 mm were found. A uniformly distributed lateral load acting in sequence was then considered for pushover analysis, which is expressed as the block weight times the load multiplier.

The pushover curves obtained from the rigid block model for the original and settled configurations are shown in Fig. 4b). Here, α is the seismic coefficient or base shear coefficient, corresponding to the total lateral load normalized by the total vertical load; d is the relative horizontal displacement at control point C_2 calculated from the deformed configuration corresponding to support movement. The comparison shows a significant decrease of the lateral stiffness, force and ultimate displacement capacity (Fig. 4b).

Fig. 4b) also shows the comparison with the analytical curves obtained from the application of the virtual work principle to the original and displaced configurations under the assumption of rigid contacts. For the application of the virtual work principle, a CAD model of the buttressed arch was developed. The failure mechanisms used for the definition of the virtual displacement diagrams were assigned using the same position of the hinges of the numerical model. Virtual displacement diagrams were defined in the CAD model with respect to both the original and displaced configurations of the arch in order to take into account the effects of large displacements on the load multiplier. Three displaced configurations of the arch were considered for the calculation of the load multipliers by the application of the virtual work principle. The first configuration corresponds to the arch without support movements and with a lateral displacement at the top of the pier equal to 30.0 mm (i.e., 28.6 mm at the control point C_2). The other configurations were those corresponding to the arch with imposed support movements of 20.0 mm and with a relative lateral displacement equal to 0.0 and 20.0 mm. The lines passing through the points corresponding to the calculated load factors and control point displacements for the original and settled configurations closely match the curves obtained from the rigid block model with rigid contacts in Fig. 4b). A comparison is also reported in Fig. 4b) with the experimental pushover curve obtained from the tilting table tests on the original configuration. Slight differences can be noted between the experimental response and the numerical pushover curve with no-tension elastic contacts, which can be ascribed to geometric imperfections and rounded corners in the experimental mock-up, as also noted in Ref. [68].

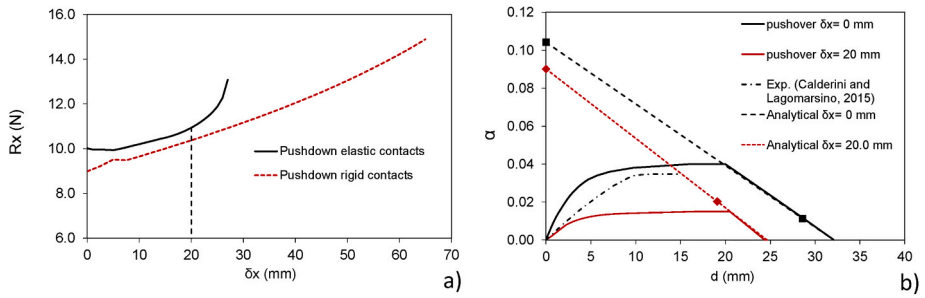

Fig. 4. Rigid block model of the buttressed arch: comparison of a) numerical pushdown and b) pushover curves with and w/o support movements.

5.2. Wall panel subjected to support movement and lateral loads

Experimental tests on a dry tuff masonry wall subjected to the combined action of support movement and lateral loads were carried out for comparisons with the proposed modeling approach of failure mechanisms involving sliding between the blocks.

The test set-up was organized according to Ref. [66] and is shown in Fig. 5. The specimen is made of a running bond panel on the right and of a block stacked prism on the left, to reproduce the interaction related to the in-plane and the out-of-plane behavior of a side-wall and of a front wall, respectively. The two parts of the panel were not interlocked, to facilitate the overturning of the block stacked prism. The dimensions of tuff blocks were 100 × 100× 50 mm and the unit weight was 12.1 kN/m^3. The average friction coefficient measured from sliding tests on two blocks stack was 0.51. The movable support was a timber table attached to two mechanical jacks for vertical movements. The entire specimen laid on a tilting table inclined by a chain puller to apply lateral loads. Two experimental tests were carried out. In the first test, the wall panel was simply investigated under the effects of lateral loads induced by the inclination of the tilting table. In the second test, a vertical downward displacement δ_z of 50 mm was applied at the movable support at first. Afterwards, the tilting table was inclined up the motion onset of the block stack. The tangent of inclination angle of the tilting table at the onset of motion corresponds to the lateral load multiplier. The load multipliers obtained from experimental tests without and with support movement were equal to 0.19 and 0.14, respectively.

For numerical simulations, sequential pushdown and pushover analyses with rigid contacts were carried out. The block corners were rounded by a radius of 10 mm. Numerical failure mechanisms compare fairly well with those observed in experimental tests (Fig. 6a, b, d). For the model with support movement $\delta_z = 50.0$ mm, the numerical value of the reaction R at the movable block is 129 N and the displacement at the top of the block stacked prism is 50.0 mm. The experimental failure load multipliers with and without support movement at the onset of motion are compared with those obtained from numerical analysis in Fig. 6c. The comparison shows a good agreement between failure load multipliers for $\delta_z = 0.0$ mm. Conversely, the experimental multiplier is slightly underestimated in the case of $\delta_z = 50.0$ mm. This is likely due to interlocking at block vertices between the block stack and the adjacent blocks of the wall panel which was observed in the case of the experimental tests with support movements.

6. Applications to rocking dynamics of single and multi-block structures

Applications to rocking dynamics are presented in this section to evaluate the accuracy and computational efficiency of the novel formulation proposed for nonlinear time-history with no-tension elastic contacts. The first application is aimed at validating the dynamic response predicted for the free-standing wall subjected to free rocking motion and pulse type excitations. In this case the response obtained from the proposed approach is compared with the results obtained from finite element modeling. Comparisons with the solution of the equation of motion in the case of the single block with rigid contact are also presented. The second case study is the dry-joint buttressed arch presented in Sect. 5. The results from experimental tests on the shaking table are herein compared with those obtained from time history analysis using no-tension elastic contacts.

6.1. Free standing walls subjected to free rocking motion and pulse-type excitation

The configuration of the rigid block model used to analyze the rocking response of the free-standing block is shown in Fig. 7a). A support block is used to apply the seismic excitation. The joints between the two rigid blocks and between the support block and the ground are discretized with four contact interfaces each. A frictionless behavior is assumed for the contact with the ground whereas a friction coefficient equal to 0.7 is assumed between the two blocks to prevent sliding failures.

The case study of the single block numerically investigated in Ref. [78] was considered at first to validate the proposed approach in the case of free rocking motion. The dimensions of the examined block are $B_1 = 0.6$ m, $H_1 = 4.2$ m. The ratio ω/φ of the initial and slenderness angle is equal to 0.5 (Fig. 7a). In order to validate a viscous damping model that is able to reproduce the energy loss and ensure dynamic equivalence with the classical rocking theory, the authors compared the analytical solution by Ref. [79] with that obtained using different software codes, including ABAQUS, DIANA and 3DEC. For the analytical solution, the authors considered the angular coefficient of restitution e corresponding to the conservation of angular momentum at impacts ($e = 0.97$). The comparison of the proposed model with the analytical and viscous damping models implemented in ABAQUS is presented in Fig. 8a). For the proposed model, the responses obtained using both rigid contacts and elastic contact with joint stiffness k_{jn} equal to 5e8 kN/m^3 are shown. The unit weight considered for numerical simulations was 18.0 kN/m^3. The friction coefficient and the time step size used for numerical simulations were set equal to 0.7 and 0.001 s, respectively. The two responses are very similar and are in a good agreement with numerical curves obtained from Ref. [78]. Similar to other numerical responses reported in Ref. [78], slight differences with the analytical solution can be noted in the plot of rotation histories for lower rocking angles, corresponding to a faster dissipation of energy.

Further comparisons with experimental tests on the free rocking motion of specimen 2 reported in Ref. [80] are presented in Fig. 8b). The dimensions of the block are $B_1 = 0.17$ m, $H_1 = 1.0$ m, the unit weight is 26.7 kN/m^3 and the friction coefficient is 0.58. The ratio ω/φ at the beginning of motion is 0.64. The numerical response closely matches the experimental one for $k_{jn} =$ 5e6 kN/m^3. The rotation time-history

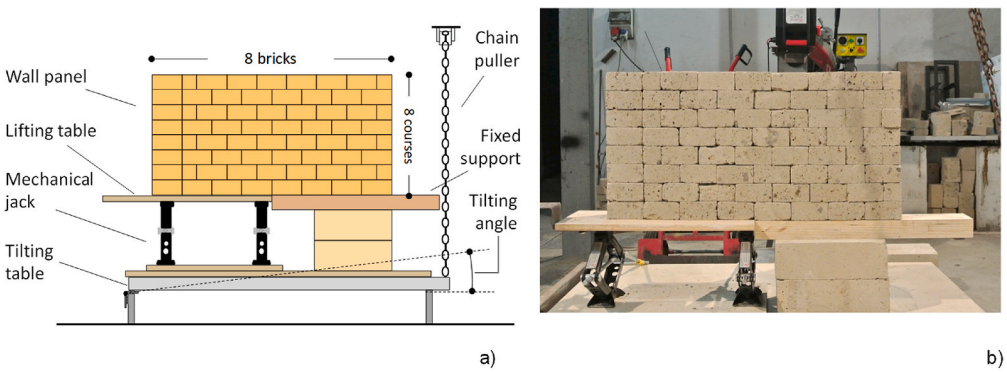

Fig. 5. Dry-joint wall panel on the tilting table: a) test set-up; b) frontal view.

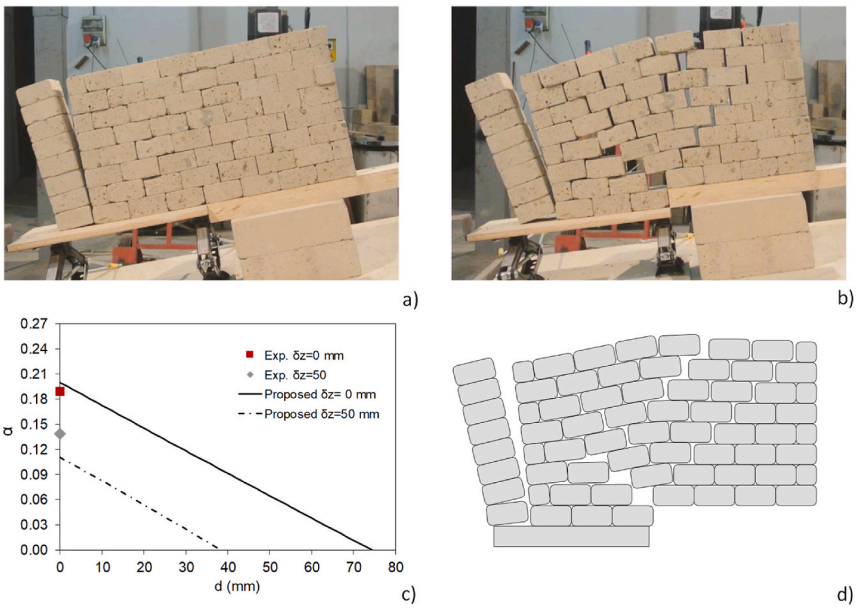

Fig. 6. a) Experimental failure mechanism at the onset of motion of the block stack without support movement and b) with vertical displacement of 50.0 mm at the movable support; c) Comparison of pushover curves with failure load multiplier at the onset of motion; d) Predicted failure mechanism under imposed displacement and lateral loads with rigid contacts.

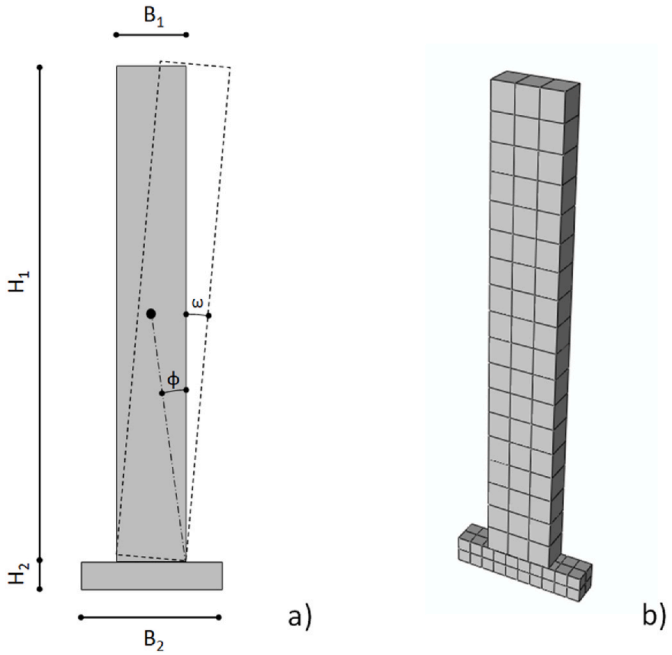

Fig. 7. a) Rigid block model of the free-standing wall and support block; b) Finite element model generated in ABAQUS.

response obtained from the model with rigid contacts is remarkably different in this case. This is also in a good agreement with the Housner solution calculated for $e = 0.95$. It should be noted that in the proposed approach the dissipation is implicitly related to the adopted time stepping scheme and is a function of the time step size and contact stiffness. A sensitivity analysis to the size of the time step was carried out both for rigid and elastic contacts to evaluate the effects on the dissipated energy (Fig. 9). The results show that in the case of elastic contacts the dissipated energy per cycle is generally lower than that corresponding to rigid contacts and increases with a larger rate for increasing values of the time step size.

To validate the proposed model in the case of base excitations and to point out the effects of contact stiffness on the rocking response, another set of simulations was carried out on the rigid block under rectangular pulse excitation. The dimensions considered for the rigid block are $H_1 = 3.5$ m, $B_1 = 0.5$ m. The stiffness of the joint k_{jn} between the two blocks was varied in the range 1.0e5 kN/m^3 ÷ 1.0e6 kN/m^3. The unit weight of the wall is 16.0 kN/m^3. A rectangular pulse excitation with magnitude equal to 0.15 g and duration 0.2 s is applied at the base block.

The finite element model of the wall-support system was generated in ABAQUS using solid elements C3D8R (Fig. 7b). The pulse excitation at the support block was assigned imposing a corresponding displacement time history as boundary condition. The general contact options were adopted for interactions with a linear formulation for normal behavior, penalty formulation for tangential behavior and a damping coefficient of 0.001. An explicit dynamic analysis was carried out. The rotation time histories obtained from the finite element and rocking block model for the two joint stiffness considered are shown in Fig. 10a), where a good agreement in terms of amplitudes and oscillations periods can be observed. To evaluate the differences in the rocking response when a rigid contact formulation is used, the response obtained from the rocking block model under the same pulse excitation is reported in Fig. 10b).

The comparison with the responses determined from the solution of the ordinary differential equation of motion and from the linearized equation by Housner are also reported for verification for $e = 0.84$. The responses under the same pulse excitation in Fig. 10 show the significant sensitivity of rotation time-histories with varying contact stiffness, both in terms of amplitudes and rocking periods.

6.2. Buttressed arch subjected to seismic excitations

The shaking table tests reported in Ref. [74] on the buttressed arch presented in Sect. 5.1 were considered to compare the time-history response in the case of a multi-block assemblage with no-tension elastic contacts. The buttressed arch was subject to a set of experimental tests with increasing value of peak ground accelerations (PGAs) up to collapse. The acceleration time series used for experimental tests was derived from the real accelerogram recorded in L'Aquila 2009 earthquake using a reduction factor $\eta_1^{-1/2}$ for time scale, being $\eta_1 = 0.1$ the geometric scale factor, so to comply with similitude requirements.

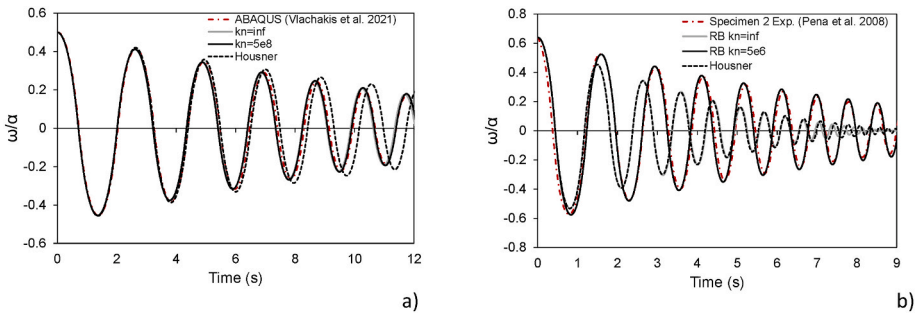

Fig. 8. a) Comparison of rotation time-histories for the rigid block model subject to free rocking motion with $B_1 = 0.6$ m, $H_1 = 4.2$ m, $\omega/\varphi = 0.5$; b) Comparison of rotation time-histories with the experimental test presented in Ref. [80].

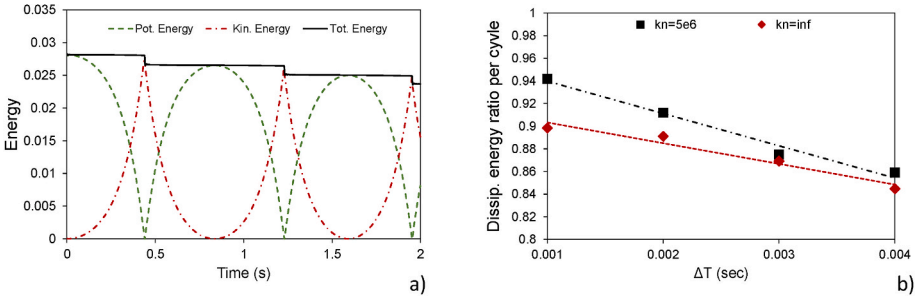

Fig. 9. Numerical analysis on the rigid block tested under free rocking motion in Ref. [80]: a) energy balance and b) sensitivity analysis of the dissipated energy per cycle to time step size and to contact stiffness.

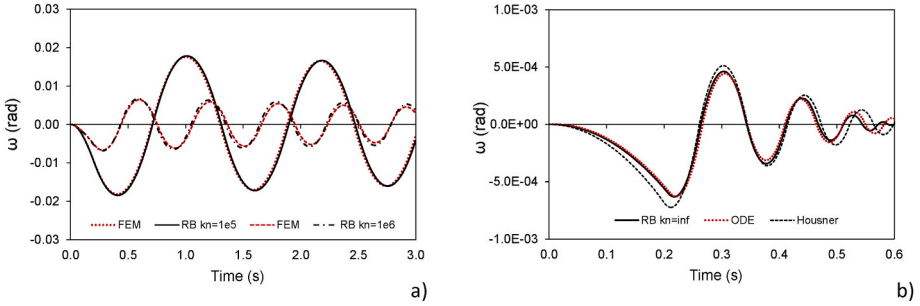

Fig. 10. Rigid block subject to rectangular pulse excitation ($B_1 = 0.5$ m, $H_1 = 3.5$ m, pulse magnitude $a_g = 0.15$ g, duration 0.2s): a) comparison of rotation time histories with rocking block and finite element model, for different joint stiffness values; b) comparison of rocking block model and ordinary differential equation solver solutions for rigid contacts.

The scaled acceleration time series AQU used in experimental tests was assigned at the base of the rigid block model for numerical analysis (Fig. 11a). The effective value of the PGA measured on the shaking table for the series considered in numerical analysis is equal 0.26 g. The size of the time increment used for numerical simulation was 0.008 s. The same mechanical parameters adopted in Sect. 5.1 for the static analysis were used for the rigid block model.

The acceleration time history at the base was applied after the transient response under the gravitational loads. The deformed configuration under the self-weight of the arch is shown in Fig. 12a).

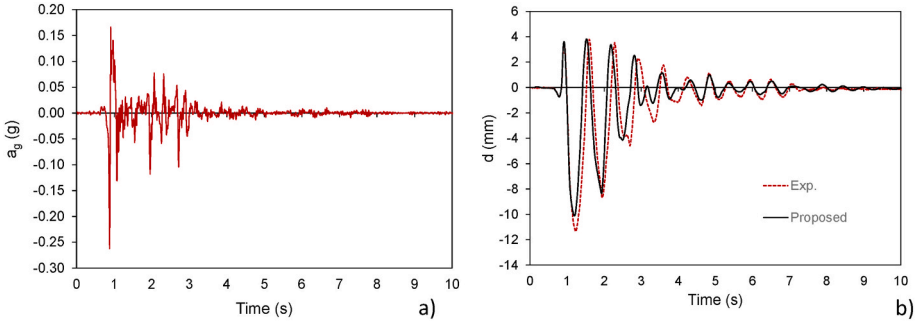

Fig. 11. a) Acceleration time history used for experimental tests on the buttressed arch; b) Comparison of displacement time histories at control point.

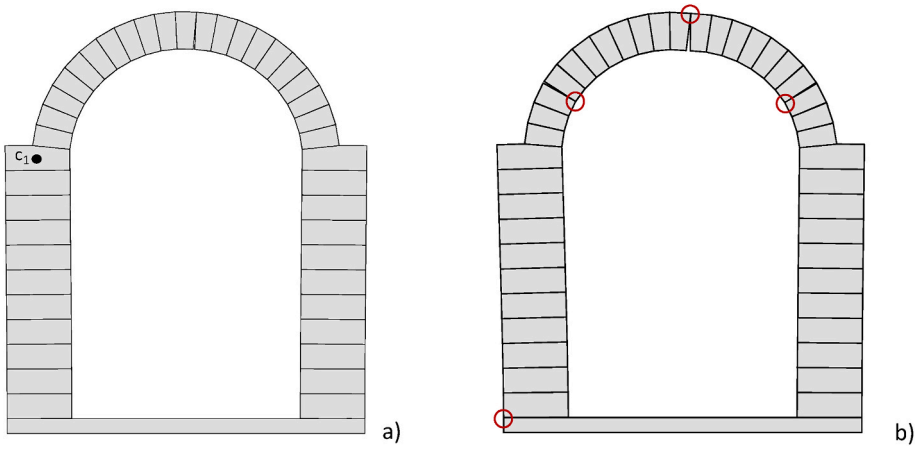

Fig. 12. Deformed configuration of the buttressed arch with no-tension elastic contacts: a) under self-weight; b) under the experimental acceleration time series at time $t = 1.28$ s (red circles indicate the hinges).

Experimental and numerical displacement time-histories at control point C_1 at the top of the left pier show good agreement both in terms of oscillations amplitudes and periods (Fig. 11b). The position of the hinges of the rocking mechanism is also in good agreement with experimental behavior (Fig. 12b).

7. Static and dynamic analysis of a triumphal arch subject to combined settlement and seismic actions

To evaluate the applicability of the proposed modeling approach on a full scale macroelement, the protype of the dry-stone triumphal arch shown in Fig. 13a) was considered. The depth of the arch is 0.60 m. The piers of the 2D-model are representative of the two lateral nave walls with depth equal to 5.50 m (shaded blocks in dark grey color in Fig. 13a). The model also comprises eight blocks at the top which correspond to the timber beams of the roof (in red color in Fig. 13a), perpendicular to the triumphal arch. The unit weight is 16.0 kN/m^3 and the friction coefficient μ is 0.65. The joint normal stiffness k_{jn} was set equal to 5.33e6 kN/m^3, corresponding to a value of the masonry Young modulus of 1600 MPa and to a block height of 300 mm. For the roof loads, a vertical force of 9.1 kN was applied at each of block representing the timber beams of the roof. The arch was subjected to a foundation movement at the right pier with equal horizontal and vertical values, and to lateral loads induced by seismic action. For the seismic action, the AQA.HNN acceleration time history was considered [81]. The time series was recorded at L'Aquila during the earthquake on April 6, 2009 and corresponds to a peak ground acceleration of 0.44 g. Two different types of analysis were carried out for seismic actions, namely a nonlinear static analysis and a time history analysis under earthquake excitation. The results are compared in terms of peak ground acceleration (PGA) at incipient collapse. In the case of pushover analysis, the values of peak ground accelerations are derived according to the displacement-based assessment procedure contained in the Italian technical standard, which is based on the capacity spectrum method.

7.1. Influence of settlements on the seismic capacity by pushover analysis

A pushdown analysis was carried out at first to evaluate the effects of movement at the right support and to assess the ultimate displacement capacity under imposed settlements. The pushdown curves expressing

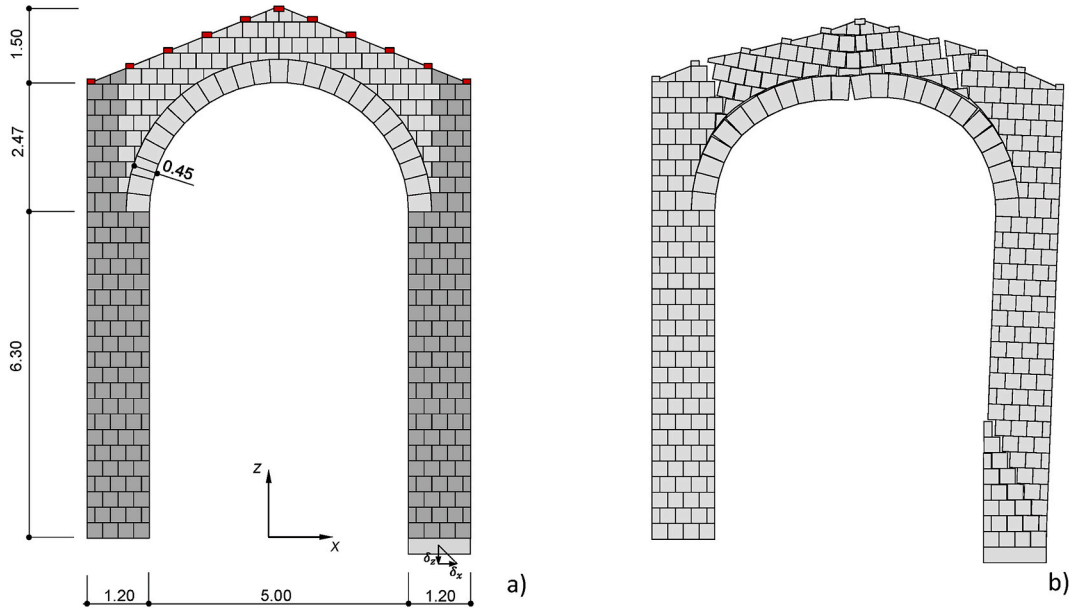

Fig. 13. a) Configuration of the prototype triumphal arch; b) Failure mechanism obtained from pushover analysis with rigid contacts under imposed movements $\delta_x = \delta_z = 150$ mm and uniformly distributed lateral loads.

the reaction components as a function of the corresponding displacement components are shown in Fig. 14. The results show that the maximum displacement capacity is attained at $\delta_{0,x} = \delta_{0,z} = 250$ mm. For sequential support movement and pushover analysis, horizontal and vertical components equal to 150 mm were applied, corresponding to 60% of the ultimate displacement. Using a displacement increment at support equal to 10 mm, the analyses took about 2 min to run on a processor Intel(R) Core(TM) i7-9850H CPU @ 2.60 GHz, with 16 GB Ram. The comparison of the pushover curves without and with imposed support movements is shown in Fig. 15a). The failure mechanisms of the triumphal arch without and with support movement are similar and correspond to a four-hinge collapse mode, with one hinge at the base involving the rotation of the right wall and three hinges in the arch (Fig. 13b).

The results of pushover analysis were used to assess the peak ground acceleration capacity corresponding to the near-collapse limit state (NCLS) according to the displacement-based assessment method contained in the Italian technical standard (Fig. 15b). The pushover curves were approximated by a trilinear model according to Ref. [82]. The secant stiffness was calculated at $0.4\alpha_u$, being α_u the load factor corresponding to the force capacity on the nonlinear pushover curve. The load factor α_y of the trilinear model was set equal to $0.9\alpha_u$. The capacity curve is obtained from the pushover curve using spectral transformation factors to convert load multipliers and displacements into corresponding spectral values. The spectral acceleration of the capacity curve is $a^* = \frac{\alpha(d_C)}{e^*} g$, where: $e^* = \frac{(\sum P_i \delta_{x,i})^2}{\sum P_i \sum (P_i \delta_{x,i}^2)}$ is the ratio of participating mass; d_C is the displacement of the control point; $\delta_{x,i}$ are the horizontal displacements corresponding to the failure mode. The spectral displacement is $d^* = d_C \Gamma^*$, where $\Gamma^* = \frac{\sum P_i \delta_{x,i}^2}{\delta_{x,C} \sum P_i \delta_{x,i}}$ is the spectral transformation factor for displacements. Load factors, corresponding displacement values and spectral transformation factors are reported in Table 1. The initial period was calculated as follows: $T_0 = 2\pi \sqrt{\frac{d_y^*}{a_y^*}}$.

The acceleration capacity at collapse is evaluated by scaling the acceleration-displacement response spectrum corresponding to the seismic input (*NC RS* in Fig. 15b) so to comply with the ultimate displacement on the capacity curve of the equivalent single degree of freedom system. In particular, the peak ground acceleration capacity $a_{g,NC}$ at the near-collapse limit state was determined from the response spectrum corresponding to the spectral acceleration $S_e(T_{NC}) = \frac{4\pi^2}{T_{CLS}^2} d_{NC}^*$, where: d_{NC}^* is the spectral displacement corresponding to NCLS, set equal to 0.6 d_0^*, being d_0^* the ultimate displacement; $T_{NC} = 1.56\pi \sqrt{\frac{d_{NC}^*}{a_{NC}^*}}$ is the corresponding period.

The predicted values of peak ground accelerations at collapse limit state without and with support movement are also reported in Table 1. The application of the assessment procedure returns quite high values of the peak ground accelerations at collapse which can be mainly ascribed to the small displacement demand associated to the elastic response spectrum. Still, the reduction of seismic capacity due to the support movement is about 12% and should not be neglected.

7.2. Influence of settlements on the dynamic response

Incremental dynamic analysis was carried out, both for the original and settled configuration, with increasing scale factors of the acceleration time series up to the collapse of the arch. The scale factors *s.f.* of the original L'Aquila record were varied in the range 0.5–0.75, corresponding to PGA of 0.22–0.33 g. The time interval 15–22s corresponding to the main shock was considered for time-history analysis. The size of the time step adopted for numerical simulations was 0.005s. With this time increment, the analyses took about 43 min to run.

Fig. 16 shows the comparison of displacement time history without and with imposed support movements under the scaled acceleration time series. The results show that the peak ground accelerations at collapse are equal to 0.33 g and 0.26 g, respectively. A stronger reduction of capacity is found in this case (21%).

The deformed configurations without and with support movement for the scale factor of 0.58 are shown in Fig. 17. In the case of the arch without support movement, the earthquake induces a spreading of the arch supports with control displacement oscillating between 100 and 160 mm with periods of about 1 s, according to the elastic period T_0 estimated with static analysis (Fig. 16a). Conversely, the arch subject to support movements $\delta_x = \delta_z = 150$ mm progressively collapses under the considered earthquake excitation, with a five-hinge failure mechanism.

The difference between PGAs at collapse obtained from time-history and pushover analysis is significative and should be ascribed to the different predicted failure mechanisms and displacement demands. Indeed, in the case of time-history analyses the displacement demand appears to be affected by the five-hinge failure mechanism (rather than by the four-hinge failure mechanism obtained from pushover analysis), which also involves disaggregation of the walls under the cyclic response (Fig. 17).

8. Conclusions

A rigid block modeling approach was presented for seismic analysis of dry-joint masonry structures which have been previously damaged by settlements. The approach is based on the solution of optimization problems which are equivalent to the set of equations governing the nonlinear static and dynamic response. The model comprises both no-tension rigid and elastic contacts and can be used to perform pushover and time history analysis on structures subjected to support movements.

Different applications were presented, including analytical, numerical and experimental tests to evaluate the accuracy of the implemented modeling approach. For the buttressed arch, the predicted pushover curves showed that the lateral stiffness, the force and the displacement capacity are significantly affected by support movements. The analytical curves derived to validate the post-peak response corresponding to rocking behavior through the application of the principle of virtual works closely match the numerical response with rigid contacts. The experimental curve obtained from tilting tests on the original

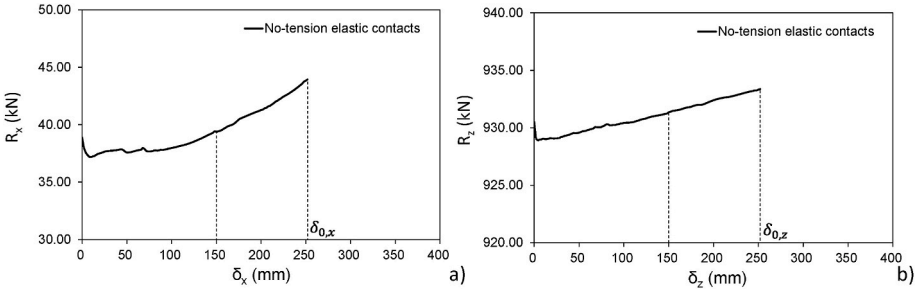

Fig. 14. a) Horizontal and b) vertical components of support reaction under imposed foundation movement.

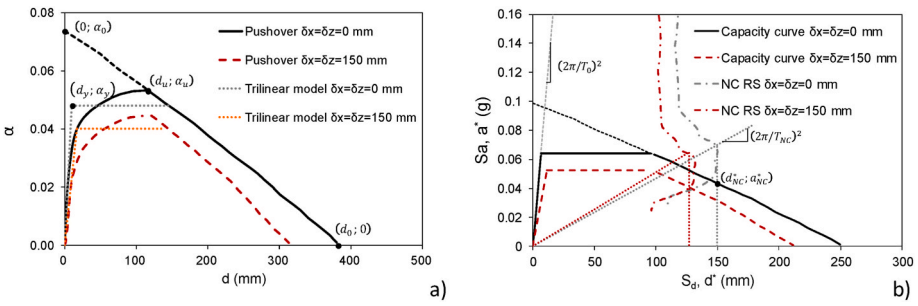

Fig. 15. a) Pushover curves of the prototype triumphal arch in the original and settled configuration and b) scheme of the capacity spectrum method used for the assessment of the peak ground acceleration at collapse limit state.

Table 1
Triumphal arch subject to support movement and lateral loads. Parameters obtained from numerical simulations for pushover and capacity curves.

	Triumphal arch w/o support movement	Triumphal arch with support movement
Model size ($b \times c$)	362 × 3996	362 × 3996
α_0	0.074	0.067
α_y	0.048	0.040
d_y (mm)	10	17
d_0 (mm)	380	313
e^*	0.75	0.77
Γ^*	0.66	0.68
d^*_{NC} (mm)	150	127
T_0 (s)	0.64	0.94
T_{NC} (s)	2.93	2.81
$a_{g,NC}$ (g)	1.13	0.99

configuration also compares well with the numerical response with no-tension elastic contacts, with differences that can be ascribed to geometric imperfections of the tested specimen.

The results of numerical analysis on the wall panel tested on the tilting table against support movement and lateral loads also showed a good agreement in terms of failure modes. Small differences of the lateral load multiplier at the onset of motion should be ascribed to interlocking of tuff blocks.

The set of analysis which was carried out to validate the seismic response with elastic contacts also showed a good agreement with numerical and experimental tests. The sensitivity analysis showed that in the proposed formulation the energy dissipation is implicitly related to algorithm and mechanical parameters. Therefore, a few preliminary numerical tests were necessary for the evaluation of dissipated energy and to discuss the sensitivity of the response of the proposed model for the case studies considered.

The application to the model of a triumphal arch showed that the proposed approach can be conveniently used to predict the static and dynamic response of full-scale macro-elements for seismic assessment under imposed support movements. The results of time-history analysis showed that, for support movement equal to 60% of ultimate displacement, the peak ground acceleration at collapse is affected by about 21%, which is not negligible and stresses the relevance of the current building condition in the seismic safety assessment. In the case of static analysis, differences of about 12% between the configurations without and with settlements were obtained. However, the peak ground accelerations at collapse obtained from pushover analysis and from the application of the displacement-based assessment method contained in the Italian technical standard were significantly higher than those obtained from time history analysis. The difference can be ascribed to the different predicted failure mechanisms, corresponding to a four-hinge and to a five-hinge collapse mode in the case of pushover and time history analysis, respectively. The disaggregation failure of the walls associated to the cyclic response also affected the seismic capacity in the case of dynamic analysis.

Reproducibility of the article's content

The authors make available the code DynABlock_2D, which was implemented for the numerical analyses presented in this study, at the following permanent repository: https://doi.org/10.5281/zenodo.6657392.

CRediT authorship contribution statement

F.P.A. Portioli: Conceptualization, Methodology, Investigation, Software, Validation, Writing – original draft, Writing – review & editing. **L. Cascini:** Investigation, Writing – review & editing. **R. Landolfo:** Supervision, Writing – review & editing. **P.B. Lourenço:** Conceptualization, Resources, Supervision, Writing – review & editing.

Declaration of competing interest

The authors declare that they have no known competing financial interests or personal relationships that could have appeared to influence the work reported in this paper.

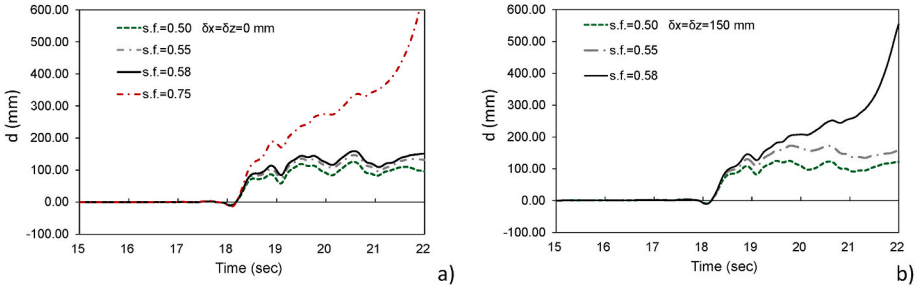

Fig. 16. Displacement time-history at control point a) without and b) with imposed movement at support.

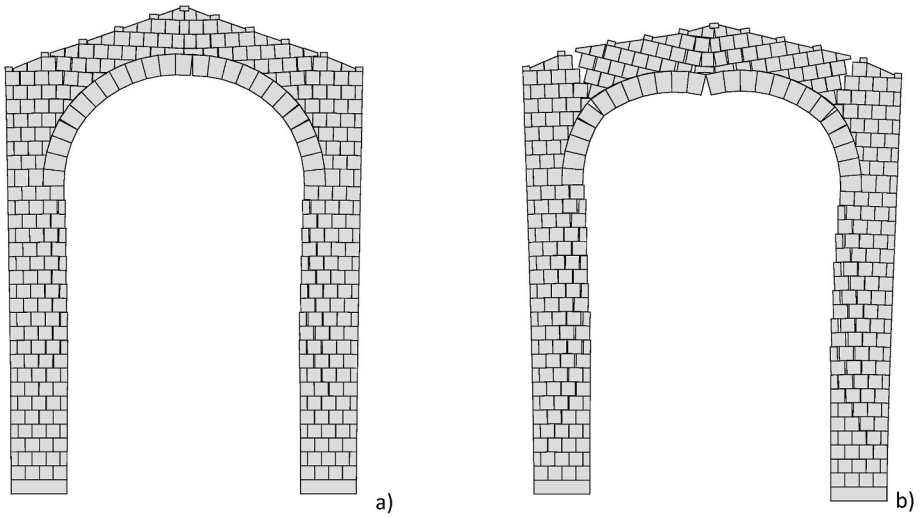

Fig. 17. Deformed configurations from time-history analysis using no-tension elastic contacts at time $t = 21.5$s: a) without and b) with imposed movement at support.

Data availability

Data will be made available on request.

Acknowledgements

The financial support of the research project DPC-ReLUIS 2022–2024: Work Package 5 'Integrated and low-impact strengthening interventions' funded by the Civil Protection Department IT (Grant no. 897-01/04/2022) is acknowledged. The authors are grateful to Prof. Chiara Calderini from the University of Genova for providing data from the experimental tests on the arch-pillars system investigated in the manuscript. The authors are also grateful to Mr. Domenico Imperatrice from the Department of Structures for Engineering and Architecture for his assistance and support throughout the experimental investigation on the wall panels subjected to support movement and lateral loads.

List of symbols

α	live load multiplier
α_0	load multiplier at the onset of the mechanism with rigid contacts
α_y	load multiplier at the force capacity with elastic contacts
Γ^*	transformation factor for spectral displacements
$\lambda_{sk+}, \lambda_{sk+}, \lambda_{ok}$	flow multipliers for positive, negative sliding and opening at contact point k
$\boldsymbol{\lambda}$	vector of flow multipliers
μ	friction coefficient
a_0^*	spectral acceleration for the onset of failure mechanisms
$\boldsymbol{A_0}$	equilibrium matrix
b	number of blocks
c	number of contact points
$\boldsymbol{c_k}, \boldsymbol{c}$	vectors of contact forces at point k and at all contact points
$C_{kn}, C_{kt}, \boldsymbol{C}$	normal, tangential contact compliance and matrix of contact compliances
d, d_y, d_0	displacement at a control point, displacement at the elastic limit and displacement capacity
d^*, d^*_{NC}	spectral displacement, spectral displacements at near collapse limit state
d_j	depth of contact joint j
e	angular coefficient of restitution at impacts
e_k	normal elastic interpenetrations at contact point k
$\boldsymbol{e}$	vector of tangential elastic deformations and normal elastic interpenetrations at contact points
e^*	ratio of participating mass
f_{xi}, f_{zi}, f_{oi}	external load components at centroid of block i
$\boldsymbol{f}, \boldsymbol{f_D}, \boldsymbol{f_L}$	vectors of external loads, dead (vertical) and live loads
g_{0k}	initial known contact gap at contact point k
$\boldsymbol{g_0}$	vector collecting initial known tangential displacement rates and gaps
$\boldsymbol{K}$	matrix of contact stiffnessesk_n,
k_t	normal and tangential stiffness at contact points
k_{jn}, k_{jt}	normal and tangential stiffness at joints
l_j	length of contact joint j
n_k, t_k, t_{0k}	normal, tangential contact forces and initial known tangential force at contact point k
$\boldsymbol{r}$	vector of constant terms associated to failure conditions
T_0, T_{NC}	equivalent periods corresponding to d_y^* and d_{NC}^*

$\boldsymbol{x_0}, \boldsymbol{x}$ vectors of initial (known) and new (unknown) positions at block centroids
y_{sk+}, y_{sk-}, y_{0k} failure conditions for positive, negative sliding and opening at contact point k
$\boldsymbol{y_k}, \boldsymbol{y}$ vectors of failure conditions at contact point k and at all contact points
$\boldsymbol{Y_k}, \boldsymbol{Y}$ flow rule matrices at contact point k and at all contact points
$\Delta u_{nk}, \Delta u_{tk}$ normal and tangential relative displacements at contact point k
$\Delta \boldsymbol{u}$ vector of local relative displacements at contact points
$\Delta x_i, \Delta z_i, \Delta \omega_i$ displacements at centroid of block i
$\Delta \boldsymbol{x}$ vector of displacements at block centroids

References

[1] Amorosi A, Boldini D, De Felice G, Malena M, Sebastianelli M. Tunnelling-induced deformation and damage on historical masonry structures. Geotechnique 2014;64:118–30. https://doi.org/10.1680/geot.13.P.032.

[2] Foraboschi P. Specific structural mechanics that underpinned the construction of Venice and dictated Venetian architecture. Eng Fail Anal 2017;78:169–95. https://doi.org/10.1016/j.engfailanal.2017.03.004.

[3] Ferrero C, Cambiaggi L, Vecchiattini R, Calderini C. Damage assessment of historic masonry churches exposed to slow-moving landslides. Int J Architect Herit 2021;15:1170–95.

[4] Nicodemo G, Ferlisi S, Peduto D, Aceto L, Gullà G. Damage to masonry buildings interacting with slow-moving landslides: a numerical analysis. Lecture Notes in Civil Engineering 2020. https://doi.org/10.1007/978-3-030-21359-6_6.

[5] Sangirardi M, Amorosi A, de Felice G. A coupled structural and geotechnical assessment of the effects of a landslide on an ancient monastery in Central Italy. Eng Struct 2020;225. https://doi.org/10.1016/j.engstruct.2020.111249.

[6] Fotopoulou SD, Pitilakis KD. Fragility curves for reinforced concrete buildings to seismically triggered slow-moving slides. Soil Dynam Earthq Eng 2013;48:143–61. https://doi.org/10.1016/j.soildyn.2013.01.004.

[7] Mele A, Miano A, Di Martire D, Infante D, Ramondini M, Prota A. Potential of remote sensing data to support the seismic safety assessment of reinforced concrete buildings affected by slow-moving landslides. Arch Civ Mech Eng 2022;22. https://doi.org/10.1007/s43452-022-00407-7.

[8] Negulescu C, Ulrich T, Bailis A, Seyedi DM. Fragility curves for masonry structures submitted to permanent ground displacements and earthquakes. Nat Hazards 2014;74:1461–74. https://doi.org/10.1007/s11069-014-1253-x.

[9] Couto R, Bento R, Gomes RC. Seismic performance and fragility curves of historical residential buildings in Lisbon downtown affected by settlements. Bull Earthq Eng 2020;18:5281–307. https://doi.org/10.1007/s10518-020-00906-z.

[10] Lagomarsino S, Penna A, Galasco A, Cattari S. TREMURI program: an equivalent frame model for the nonlinear seismic analysis of masonry buildings. Eng Struct 2013;56:1787–99. https://doi.org/10.1016/j.engstruct.2013.08.002.

[11] Lourenço PB, Mendes N, Ramos LF, Oliveira DV. Analysis of masonry structures without box behavior. Int J Architect Herit 2011;5:369–82. https://doi.org/10.1080/15583058.2010.528824.

[12] Lagomarsino S. Seismic assessment of rocking masonry structures. Bull Earthq Eng 2015;13:97–128. https://doi.org/10.1007/s10518-014-9609-x.

[13] DeJong MJ. Settlement effects on masonry structures. In: Structural analysis of historical constructions: anamnesis, diagnosis, therapy, controls - proceedings of the 10th international conference on structural analysis of historical constructions. SAHC; 2016. p. 449–56. 2016.

[14] Ferrero C, Calderini C, Roca P. Experimental response of a scaled dry-joint masonry arch subject to inclined support displacements. Eng Struct 2022;253. https://doi.org/10.1016/j.engstruct.2021.113804.

[15] Di Carlo F, Coccia S, Rinaldi Z. Collapse load of a masonry arch after actual displacements of the supports. Arch Appl Mech 2018;88:1545–58. https://doi.org/10.1007/s00419-018-1386-6.

[16] Di Carlo F, Coccia S. Collapse state of elliptical masonry arches after finite displacements of the supports. Eng Fail Anal 2020;114.

[17] Ochsendorf JA. The masonry arch on spreading supports. Struct Eng 2006;84:29–35.

[18] Zampieri P, Cavalagli N, Gusella V, Pellegrino C. Collapse displacements of masonry arch with geometrical uncertainties on spreading supports. Comput Struct 2018;208:118–29. https://doi.org/10.1016/j.compstruc.2018.07.001.

[19] Galassi S, Misseri G, Rovero L. Capacity assessment of masonry arches on moving supports in large displacements: numerical model and experimental validation. Eng Fail Anal 2021;129. https://doi.org/10.1016/j.engfailanal.2021.105700.

[20] Galassi S, Misseri G, Rovero L, Tempesta G. Analysis of masonry pointed arches on moving supports: a numeric predictive model and experimental evaluations. Lecture Notes in Mechanical Engineering 2020. https://doi.org/10.1007/978-3-030-41057-5_163.

[21] D'Altri AM, Sarhosis V, Milani G, Rots J, Cattari S, Lagomarsino S, Sacco E, Tralli A, Castellazzi G, de Miranda S. Modeling strategies for the computational analysis of unreinforced masonry structures: review and classification. Arch Comput Methods Eng 2020;27:1153–85. https://doi.org/10.1007/s11831-019-09351-x.

[22] Roca P, Cervera M, Gariup G, Pela' L. Structural analysis of masonry historical constructions. Classical and advanced approaches. Arch Comput Methods Eng 2010;17:299–325. https://doi.org/10.1007/s11831-010-9046-1.

[23] da Silva LCM, Milani G. A FE-based macro-element for the assessment of masonry structures: linear static, vibration, and non-linear cyclic analyses. Appl Sci 2022;12. https://doi.org/10.3390/app12031248.

[24] Ferrero C, Calderini C, Roca P. Effect of joint deformability on the experimental and numerical response of dry-joint masonry arches subjected to large support displacements. Eng Struct 2023;275. https://doi.org/10.1016/j.engstruct.2022.115236.

[25] Lasciarrea WG, Amorosi A, Boldini D, de Felice G, Malena M. Jointed Masonry Model: a constitutive law for 3D soil-structure interaction analysis. Eng Struct 2019;201. https://doi.org/10.1016/j.engstruct.2019.109803.

[26] Malena M, de Felice G, Marfia S. AnMas: anisotropic strength domain for masonry. Eng Struct 2022;257. https://doi.org/10.1016/j.engstruct.2022.114050.

[27] Pantò B, Chisari C, Macorini L, Izzuddin BA. A hybrid macro-modelling strategy with multi-objective calibration for accurate simulation of multi-ring masonry arches and bridges. Comput Struct 2022;265. https://doi.org/10.1016/j.compstruc.2022.106769.

[28] Milani G. Simple lower bound limit analysis model for masonry double curvature structures. Comput Struct 2022;269. https://doi.org/10.1016/j.compstruc.2022.106831.

[29] Angelillo M, Fortunato A, Gesualdo A, Iannuzzo A, Zuccaro G. Rigid block models for masonry structures. Int. J. Mason. Res. Innov. 2018;3:349–68. https://doi.org/10.1504/IJMRI.2018.095701.

[30] Iannuzzo A, Dell'Endice A, Van Mele T, Block P. Numerical limit analysis-based modelling of masonry structures subjected to large displacements. Comput Struct 2021;242. https://doi.org/10.1016/j.compstruc.2020.106372.

[31] Jiménez Rios A, Nela B, Pingaro M, Reccia E, Trovalusci P. Rotation and sliding collapse mechanisms for in plane masonry pointed arches: statistical parametric assessment. Eng Struct 2022;262. https://doi.org/10.1016/j.engstruct.2022.114338.

[32] Jiménez Rios A, Pingaro M, Reccia E, Trovalusci P. Statistical assessment of in-plane masonry panels using limit analysis with sliding mechanism. J Eng Mech 2022;148. https://doi.org/10.1061/(ASCE)EM.1943-7889.0002061.

[33] Pepe M, Sangirardi M, Reccia E, Pingaro M, Trovalusci P, de Felice G. Discrete and continuous approaches for the failure analysis of masonry structures subjected to settlements. Front. Built Environ. 2020;6. https://doi.org/10.3389/fbuil.2020.00043.

[34] Pepe M, Pingaro M, Trovalusci P, Reccia E, Leonetti L. Micromodels for the in-plane failure analysis of masonry walls: limit analysis, FEM and FEM/DEM approaches. Frat Ed Integrità Strutt 2020;14:504–16. https://doi.org/10.3221/IGF-ESIS.51.38.

[35] Giouvanidis AI, Dimitrakopoulos EG, Lourenço PB. Chattering: an overlooked peculiarity of rocking motion. Nonlinear Dynam 2022. https://doi.org/10.1007/s11071-022-07578-1.

[36] Giresini L, Solarino F, Paganelli O, Oliveira DV, Froli M. ONE-SIDED rocking analysis of corner mechanisms in masonry structures: influence of geometry, energy dissipation, boundary conditions. Soil Dynam Earthq Eng 2019;123:357–70. https://doi.org/10.1016/j.soildyn.2019.05.012.

[37] Mehrotra A, DeJong MJ. The influence of interface geometry, stiffness, and crushing on the dynamic response of masonry collapse mechanisms. Earthq Eng Struct Dynam 2018;47:2661–81. https://doi.org/10.1002/eqe.3103.

[38] Calò M, Malomo D, Gabbianelli G, Pinho R. Shake-table response simulation of a URM building specimen using discrete micro-models with varying degrees of detail. Bull Earthq Eng 2021;19:5953–76. https://doi.org/10.1007/s10518-021-01202-0.

[39] Casolo S. Macroscale modelling of the orthotropic shear damage in the dynamics of masonry towers by RBSM. Eng Fail Anal 2021;130. https://doi.org/10.1016/j.engfailanal.2021.105744.

[40] Galassi S, Ruggieri N, Tempesta G. A novel numerical tool for seismic vulnerability analysis of ruins in archaeological sites. Int J Architect Herit 2020;14:1–22. https://doi.org/10.1080/15583058.2018.1492647.

[41] Malomo D, Pinho R, Penna A. Applied element modelling of the dynamic response of a full-scale clay brick masonry building specimen with flexible diaphragms. Int J Architect Herit 2020;14:1484–501. https://doi.org/10.1080/15583058.2019.1616004.

[42] D'Altri AM, Lo Presti N, Grillanda N, Castellazzi G, de Miranda S, Milani G. A two-step automated procedure based on adaptive limit and pushover analyses for the seismic assessment of masonry structures. Comput Struct 2021;252. https://doi.org/10.1016/j.compstruc.2021.106561.

[43] Foraboschi P, Vanin A. Non-linear static analysis of masonry buildings based on a strut-and-tie modeling. Soil Dynam Earthq Eng 2013;55:44–58. https://doi.org/10.1016/j.soildyn.2013.08.005.

[44] Funari MF, Mehrotra A, Lourenço PB. A tool for the rapid seismic assessment of historic masonry structures based on limit analysis optimisation and rocking

dynamics. Appl Res Engl Lang 2021;11:1–22. https://doi.org/10.3390/app11030942.
[45] Malena M, Angelillo M, Fortunato A, de Felice G, Mascolo I. Arch bridges subject to pier settlements: continuous vs. piecewise rigid displacement methods. Meccanica 2021;56:2487–505. https://doi.org/10.1007/s11012-021-01397-1.
[46] Scacco J, Grillanda N, Milani G, Lourenço PB. Novel non-linear static numerical model for curved masonry structures based on a combined adaptive limit analysis and discrete FE computations. Int J Solid Struct 2022:236–7. https://doi.org/10.1016/j.ijsolstr.2021.111265.
[47] Bui T-T, Limam A, Sarhosis V. Failure analysis of masonry wall panels subjected to in-plane and out-of-plane loading using the discrete element method. Eur. J. Environ. Civ. Eng. 2021;25:876–92. https://doi.org/10.1080/19648189.2018.1552897.
[48] Bui TT, Limam A, Sarhosis V, Hjiaj M. Discrete element modelling of the in-plane and out-of-plane behaviour of dry-joint masonry wall constructions. Eng Struct 2017;136:277–94. https://doi.org/10.1016/j.engstruct.2017.01.020.
[49] Kassotakis N, Sarhosis V, Riveiro B, Conde B, D'Altri AM, Mills J, Milani G, de Miranda S, Castellazzi G. Three-dimensional discrete element modelling of rubble masonry structures from dense point clouds. Autom ConStruct 2020;119. https://doi.org/10.1016/j.autcon.2020.103365.
[50] Pulatsu B, Gonen S, Parisi F, Erdogmus E, Tuncay K, Funari MF, Lourenço PB. Probabilistic approach to assess URM walls with openings using discrete rigid block analysis (D-RBA). J Build Eng 2022;61. https://doi.org/10.1016/j.jobe.2022.105269.
[51] Sarhosis V, Bagi K, Lemos JV, Milani G. Computational modeling of masonry structures using the discrete element method. IGI Global 2016. https://doi.org/10.4018/978-1-5225-0231-9.
[52] Savalle N, Lourenço PB, Milani G. Joint stiffness influence on the first-order seismic capacity of dry-joint masonry structures: numerical DEM investigations. Appl Sci 2022;12. https://doi.org/10.3390/app12042108.
[53] Baggio C, Trovalusci P. Collapse behaviour of three-dimensional brick-block systems using non-linear programming. Struct Eng Mech 2000;10:181–95. https://doi.org/10.12989/sem.2000.10.2.181.
[54] Ferris MC, Tin-Loi F. Limit analysis of frictional block assemblies as a mathematical program with complementarity constraints. Int J Mech Sci 2001;43:209–24. https://doi.org/10.1016/S0020-7403(99)00111-3.
[55] Gilbert M, Casapulla C, Ahmed HM. Limit analysis of masonry block structures with non-associative frictional joints using linear programming. Comput Struct 2006;84:873–87. https://doi.org/10.1016/j.compstruc.2006.02.005.
[56] Livesley RK. Limit analysis of structures formed from rigid blocks. Int J Numer Methods Eng 1978;12:1853–71. https://doi.org/10.1002/nme.1620121207.
[57] Lourenço PB, Oliveira DV, Roca P, Orduña A. Dry joint stone masonry walls subjected to in-plane combined loading. J Struct Eng 2005;131:1665–73. https://doi.org/10.1061/(ASCE)0733-9445(2005)131:11(1665).
[58] Orduña A, Lourenço PB. Three-dimensional limit analysis of rigid blocks assemblages. Part I: torsion failure on frictional interfaces and limit analysis formulation. Int J Solid Struct 2005;42:5140–60. https://doi.org/10.1016/j.ijsolstr.2005.02.010.
[59] Krabbenhoft K, Lyamin AV, Huang J, Vicente da Silva M. Granular contact dynamics using mathematical programming methods. Comput Geotech 2012;43:165–76. https://doi.org/10.1016/j.compgeo.2012.02.006.
[60] Krabbenhoft K, Huang J, Da Silva MV, Lyamin AV. Granular contact dynamics with particle elasticity. Granul Matter 2012;14:607–19. https://doi.org/10.1007/s10035-012-0360-1.
[61] Meng J, Huang J, Sheng D, Sloan SW. Granular contact dynamics with elastic bond model. Acta Geotech 2017;12:479–93. https://doi.org/10.1007/s11440-016-0481-5.
[62] Cottle RW, Pang JS, Stone RE. The linear complementarity problem. SIAM; 2009.
[63] Andersen ED, Roos C, Terlaky T. On implementing a primal-dual interior-point method for conic quadratic optimization. Math. Program. Ser. B 2003;95:249–77. https://doi.org/10.1007/s10107-002-0349-3.
[64] Andersen ED, Gondzio J, Meszaros C, Xu X. Implementation of interior point methods for large scale linear programming. In: Terlaky T, editor. Interior-point methods of mathematical programming. Kluwer Academic Publishers; 1996. p. 189–252.
[65] Portioli FPA. Rigid block modelling of historic masonry structures using mathematical programming: a unified formulation for non-linear time history, static pushover and limit equilibrium analysis. Bull Earthq Eng 2020;18:211–39. https://doi.org/10.1007/s10518-019-00722-0.
[66] Gagliardo R, Portioli FPA, Cascini L, Landolfo R, Lourenço PB. A rigid block model with no-tension elastic contacts for displacement-based assessment of historic masonry structures subjected to settlements. Eng Struct 2021;229. https://doi.org/10.1016/j.engstruct.2020.111609.
[67] Portioli F, Cascini L. Large displacement analysis of dry-jointed masonry structures subjected to settlements using rigid block modelling. Eng Struct 2017;148:485–96. https://doi.org/10.1016/j.engstruct.2017.06.073.
[68] Portioli FPA, Godio M, Calderini C, Lourenço PB. A variational rigid-block modeling approach to nonlinear elastic and kinematic analysis of failure mechanisms in historic masonry structures subjected to lateral loads. Earthq Eng Struct Dynam 2021;50:3332–54. https://doi.org/10.1002/eqe.3512.
[69] Portioli F, Cascini L. Contact dynamics of masonry block structures using mathematical programming. J Earthq Eng 2018;22:94–125. https://doi.org/10.1080/13632469.2016.1217801.
[70] CIRCOLARE 21 gennaio 2019, n. 7 C.S.LL.PP. Istruzioni per l'applicazione dell'«Aggiornamento delle "Norme tecniche per le costruzioni"» di cui al decreto ministeriale 17 gennaio 2018 Official Gazette of the Italian Republic (G.U.) 2019;35(5):1–337.
[71] NTC. Decreto Ministeriale 17/1/2018: aggiornamento delle «Norme tecniche per le costruzioni». Ministry of Infrastructures and Transportations; 2018.
[72] Lloyd Smith D. Mathematical programming methods in structural plasticity. Vienna: Springer Vienna; 1990. https://doi.org/10.1007/978-3-7091-2618-9.
[73] Maier G, Nappi A. A theory of no-tension discretized structural systems. Eng Struct 1990;12:227–34. https://doi.org/10.1016/0141-0296(90)90021-J.
[74] Calderini C, Lagomarsino S, Rossi M, De Canio G, Mongelli ML, Roselli I. Shaking table tests of an arch-pillars system and design of strengthening by the use of tie-rods. Bull Earthq Eng 2015;13:279–97. https://doi.org/10.1007/s10518-014-9678-x.
[75] Calderini C, Lagomarsino S. Seismic response of masonry arches reinforced by tie-rods: static tests on a scale model. J Struct Eng 2015;141. https://doi.org/10.1061/(ASCE)ST.1943-541X.0001079.
[76] Ferrero C, Rossi M, Roca P, Calderini C. Experimental and numerical analysis of a scaled dry-joint arch on moving supports. Int. J. Mason. Res. Innov. 2021;6:405–21. https://doi.org/10.1504/IJMRI.2021.118818.
[77] Ferrero C, Calderini C, Portioli F, Roca P. Large displacement analysis of dry-joint masonry arches subject to inclined support movements. Eng Struct 2021;238. https://doi.org/10.1016/j.engstruct.2021.112244.
[78] Vlachakis G, Giouvanidis AI, Mehrotra A, Lourenço PB. Numerical block-based simulation of rocking structures using a novel universal viscous damping model. J Eng Mech 2021;147. https://doi.org/10.1061/(ASCE)EM.1943-7889.0001985.
[79] Housner GW. The behaviour of inverted pendulum structures during earthquakes. Bull Seismol Soc Am 1963;53:403–17. https://doi.org/10.1017/CBO9781107415324.004.
[80] Peña F, Lourenço PB, Campos-Costa A. Experimental dynamic behavior of free-standing multi-block structures under seismic loadings. J Earthq Eng 2008;12:953–79. https://doi.org/10.1080/13632460801890513.
[81] Luzi L, Puglia R, Russo E, ORFEUS-WG5. Engineering strong motion database. version 1.0, https://doi.org/10.13127/ESM; 2016.
[82] Doherty K, Griffith MC, Lam NTK, Wilson J. Displacement-based seismic analysis for out-of-plane bending of unreinforced masonry walls. Earthq Eng Struct Dynam 2002;31:833–50. https://doi.org/10.1002/eqe.126.